International Journal of Heat and Fluid Flow 30 (2009) 823–830

Contents lists available at ScienceDirect

International Journal of Heat and Fluid Flow

journal homepage: www.elsevier.com/locate/ijhff

Conjugate forced convection and heat conduction in circular microchannels

C. Nonino *, S. Savino, S. Del Giudice, L. Mansutti

Dipartimento di Energetica e Macchine, Università degli Studi di Udine, Via delle Scienze 208, 33100 Udine, Italy

ARTICLE INFO

Article history:
Received 25 November 2008
Received in revised form 13 March 2009
Accepted 23 March 2009
Available online 26 April 2009

Keywords:
Circular microchannels
Conjugate heat transfer
Numerical simulations

ABSTRACT

The effects of axial heat conduction in the solid walls of microchannels of circular cross-sections are analyzed here. A systematic approach is adopted, with the aim of pointing out the influence of geometrical parameters and of solid wall thermal conductivity on microchannel heat transfer. The reliability of a commonly adopted criterium, based on the so-called axial conduction number, to assess the relevance of axial heat conduction is also discussed. Numerical simulations concern the simultaneously developing laminar flow of a constant property fluid in microchannels of different length, wall thickness and wall material, heated with a uniform heat flux at the outer surface, for different values of the Reynolds number. Moreover, since often in experimental tests the two end sections of the microchannel wall are not perfectly insulated, the effects of heat losses through these sections are also considered. A hybrid finite element procedure, which implies the step-by-step solution of the parabolized momentum equations in the fluid domain, followed by the solution of the energy equation in the entire domain, corresponding to both the solid and the fluid parts, is used for the numerical simulations.

1. Introduction

In forced convection heat transfer problems involving channels of conventional size, the axial heat conduction in the duct walls can, in general, be neglected because the wall thickness is usually very small compared to the hydraulic diameter. On the contrary, in most microscale thermal devices, the area of the transverse section of the solid material perpendicular to the flow direction is comparable to the area of the channel cross-section. As a consequence, the effects of heat conduction in the solid walls cannot often be disregarded. For instance, it is well known that, if in the calculation of convective heat transfer coefficients from experimental data the effects of these conjugate heat transfer phenomena are neglected, the corresponding Nusselt numbers are, generally, underestimated (Liu et al., 2007; Celata et al., 2006; Morini, 2005). In particular, axial wall heat conduction represents one of the factors that can cause the discrepancies, often reported in scientific literature, between microchannel heat transfer data and predictions of standard correlations valid for conventional size channels (Herwig and Hausner, 2003).

Numerical simulations can give a useful support to experimental work since they allow the analysis of fluid flow and heat transfer phenomena in idealized conditions, where only few selected effects are taken into account. However, because of the enormous difference between the transverse and the longitudinal scales of the computational domain, the solution of the three-dimensional elliptic form of the Navier–Stokes equations in the portion of the domain corresponding to the flow passage requires a significant CPU time. Therefore, several researchers use simplified approaches where, for instance, a fully developed velocity field or a constant convective heat transfer coefficient are assumed in the whole microchannel (Maranzana et al., 2004; Ryu et al., 2002), but, of course, this does not allow the entrance effects to be taken into account. On the other hand, in many microchannel flows of practical interest, velocity and temperature fields develop simultaneously, resulting in overlapping hydrodynamic and thermal entrance regions. This occurs when heat transfer begins at the duct inlet, where the velocity boundary layer also starts developing. In such a situation, entrance effects on fluid flow and forced convection heat transfer cannot be neglected if, as it quite often happens in microchannel laminar flows, the total length of the duct is comparable with that of the entrance region.

In this paper, as an alternative to massive CFD, a hybrid technique, which has the advantage of accounting for all the three-dimensional features of the flow field, but with a limited computational effort, is proposed for the solution of conjugate convection-conduction heat transfer problems in microchannels. A very efficient finite element procedure is first employed for the step-by-step solution of the parabolised momentum equations in a domain corresponding to the cross-section of the duct, discretized using a sufficiently fine grid (Nonino et al., 1988, 2006). Provided that the axial diffusion of momentum can be neglected, such an approach is very advantageous with respect to the one based on the steady-state solution of the elliptic form of the Navier–Stokes equations in a three-dimensional domain corresponding to the whole duct

* Corresponding author. Tel.: +39 0432 558019; fax: +39 0432 558027.
E-mail address: carlo.nonino@uniud.it (C. Nonino).

0142-727X/$ - see front matter © 2009 Elsevier Inc. All rights reserved.
doi:10.1016/j.ijheatfluidflow.2009.03.009

Nomenclature

c	specific heat (J kg^{-1} K^{-1})
D	diameter (m)
h	convective heat transfer coefficient (W m^{-2} K^{-1})
k	thermal conductivity (W m^{-1} K^{-1})
M	axial conduction number, Eq. (10)
L	length of the microchannel (m)
$\dot{m}$	mass flow rate (kg s^{-1})
Nu	Nusselt number ($= h_i D_i/k_f$)
Nu_e	end section Nusselt number ($= h_a D_i/k_f$)
n	outward normal to the boundary (m)
Pe	Péclet number ($= Re\ Pr$)
Pr	Prandtl number ($= c_f \mu_f/k_f$)
p	deviation from the hydrostatic pressure (Pa)
q	heat transfer rate (W)
q'	heat transfer rate per unit length (Wm^{-1})
q''	heat flux (Wm^{-2})
Re	Reynolds number ($= \rho_f u_{in} D_i/\mu_f$)
r, x	cylindrical coordinates (m)
T	dimensionless temperature ($= \pi k_f (t - t_{in})/q'_o$)
t	temperature (°C)
u, v	velocity components in x and r directions (ms^{-1})
w	wall thickness (m)
X^*	dimensionless axial coordinate ($= x/D_i Pe$)

Greek letters

ϕ	correction velocity potential (m^2 s^{-1})
μ	dynamic viscosity (kg m^{-1} s^{-1})
ρ	density (kg m^{-3})

Subscripts and superscripts

a	ambient
b	bulk
e	microchannel end section
f	fluid
i	inner, fluid–solid interface
in	inlet
o	outer, outer surface
out	outlet
s	solid
w	wall
$'$	correction value
$-$	average value

because of the high value of the ratio between the total length and the hydraulic diameter. Then, the three-dimensional hydrodynamically developing velocity field thus determined is used in the finite element solution of the steady-state energy equation in the entire domain, corresponding to both the solid and the fluid parts. Before solving the energy equation, the fulfillment of the discrete mass conservation constraint for the velocity field mapped onto the new grid is obtained by solving a Poisson equation for a correction velocity potential which allows the calculation of appropriate velocity corrections. This technique is standard in the context of fractional step methods, often used in the solution of the continuity and the Navier–Stokes equations (Patankar, 1980; Gresho, 1990; Nonino, 2003). While the idea of first solving the Navier–Stokes equations only in the fluid domain and then the energy equation in both the fluid and solid domains is not new (Fakheri and Al-Bakhit, 2005; Al-Bakhit and Fakheri, 2005, 2006; Lelea et al., 2004), it must be pointed out that the mapping adopted here of the velocity field onto grids with different nodal densities allows a greater flexibility in the meshing of complex geometries.

As a first application of this procedure, the axial heat conduction in the solid walls of microchannels of circular cross-section is analyzed here, since this simple geometry is often used in experimental studies (Liu et al., 2007; Celata et al., 2006; Lelea et al., 2004; Li et al., 2007). Of course, this problem has already been considered in the past (Mori et al., 1974), but a more systematic approach is adopted in this paper, with the aim of pointing out the influence of geometrical parameters and solid wall thermal conductivity on microchannel heat transfer and of verifying the reliability of a commonly adopted criterium, based on the value of the so-called axial conduction number, to assess the relevance of axial wall heat conduction (Maranzana et al., 2004; Hetsroni et al., 2005; Celata et al., 2006; Morini, 2005; Gamrat et al., 2005; Li et al., 2007). Numerical simulations concern the simultaneously developing laminar flow of a constant property fluid in microchannels of different length, wall thickness and wall material, heated with a uniform heat flux at the outer surface, for different values of the Reynolds number. Moreover, since in experimental tests the two ends of the microchannel wall are often not perfectly insulated (Tiselj et al., 2004), the effects of heat conduction through the microchannel walls at both end sections are also considered.

2. Mathematical model

The hybrid technique described below can be employed, as an alternative to massive CFD, for the solution of steady-state conjugate convection-conduction heat transfer problems in microchannels with constant cross-sections and thick walls, provided that reference is made to a constant property fluid and that axial diffusion of momentum can be neglected (parabolic flow), which is a reasonable assumption when the Reynolds number is equal to or larger than 50 (Shah and London, 1978). In these hypotheses, microchannel flows are governed by the continuity and the parabolized form of the Navier–Stokes equations, which, with reference to the axisymmetric geometries considered in this paper, can be written as

$$\frac{\partial u}{\partial x} + \frac{1}{r}\frac{\partial}{\partial r}(rv) = 0 \tag{1}$$

$$\rho_f u \frac{\partial u}{\partial x} = \frac{\mu_f}{r}\frac{\partial}{\partial r}\left(r\frac{\partial u}{\partial r}\right) - \rho_f v \frac{\partial u}{\partial r} - \frac{d\overline{p}}{dx} \tag{2}$$

$$\rho_f u \frac{\partial v}{\partial x} = \frac{\mu_f}{r}\left[\frac{\partial}{\partial r}\left(r\frac{\partial v}{\partial r}\right) - \frac{v}{r}\right] - \rho_f v \frac{\partial v}{\partial r} - \frac{\partial p}{\partial r} \tag{3}$$

According to the assumption of a parabolic flow, all the derivatives in the axial direction are neglected in the diffusive terms of Eqs. (2) and (3) (Hirsh, 1988). In the above equations, x and r are the axial and radial coordinates, while u and v represent the axial and the radial velocity components. Finally, p is the deviation from the hydrostatic pressure, $\overline{p}$ is its average value over the cross-section, while ρ_f and μ_f represent density and dynamic viscosity of the fluid, respectively. The solution domain can be bounded by rigid walls or by the symmetry axis. On rigid boundaries the no-slip conditions, that is, $u = v = 0$, are imposed. Instead, symmetry conditions at the symmetry axis are $\partial u/\partial r = 0$ and $v = 0$. The model equations are solved using a finite element procedure based on a segregated approach which implies the sequential solution of momentum equations on a one-dimensional domain corresponding to the cross-section of

the channel. A marching method is then adopted to move forward in the axial direction (Nonino et al., 1988). The pressure–velocity coupling is dealt with using an improved projection algorithm already employed for the solution of the Navier–Stokes equations in their elliptic form (Nonino, 2003).

The velocity field, which can be determined using a very fine space resolution in the axial direction, is then mapped onto a two-dimensional grid used to discretize the complete domain of interest, corresponding to both the fluid in the microchannel and its solid walls, and to solve the elliptic form of the steady-state energy equation

$$\rho c u \frac{\partial t}{\partial x} + \rho c v \frac{\partial t}{\partial r} = k\left[\frac{1}{r}\frac{\partial}{\partial r}\left(r\frac{\partial t}{\partial r}\right) + \frac{\partial^2 t}{\partial x^2}\right] \tag{4}$$

where t is temperature and ρ, c and k represent density, specific heat and thermal conductivity, which are equal to ρ_f, c_f and k_f in the fluid and to ρ_s, c_s and k_s in the solid. On external solid boundaries, appropriate boundary conditions are of the Neumann $q'' = q''_w$ or of the convective $q'' = h_a(t - t_a)$ type, where h_a is the external convective heat transfer coefficient and t_a is the ambient fluid temperature. Symmetry conditions are $\partial t/\partial r = 0$. Finally, Dirichlet $t = t_{in}$ and Neumann $\partial t/\partial x = 0$ conditions are imposed on inflow and outflow boundaries, respectively.

As the velocity field is determined before the conjugate thermal problem is solved, the mesh employed for the solution of the energy equation in the fluid part of the domain can be significantly coarser than the mesh that would be required if the Navier–Stokes equations also had to be solved in the same domain in their elliptic form. This, of course, allows significant savings in computer time, thus making systematic studies and optimization procedures easier. However, it must be pointed out that the velocity field mapped onto a coarser grid, whose components can be indicated as u^* and v^*, in general, does not locally satisfy the discretized continuity equation. Therefore, before solving the energy equation, the appropriate velocity corrections u' and v' must be calculated to obtain a corrected velocity field u, v

$$u = u^* + u'; \quad v = v^* + v' \tag{5}$$

which satisfies the discretized form of the mass conservation constraint. To this purpose, a technique is employed here, which is standard in the context of fractional step methods, often used to solve the continuity and the Navier–Stokes equations (Patankar, 1980; Gresho, 1990; Nonino, 2003). This procedure implies the solution of the discretized form of the Poisson equation for the velocity correction potential ϕ

$$\frac{1}{r}\frac{\partial}{\partial r}\left(r\frac{\partial \phi}{\partial r}\right) + \frac{\partial^2 \phi}{\partial x^2} = -\left[\frac{\partial u^*}{\partial x} + \frac{1}{r}\frac{\partial}{\partial r}(r v^*)\right] \tag{6}$$

subjected to the boundary conditions $\partial\phi/\partial n = 0$ on the whole boundary. In addition, $\phi = 0$ must be specified in an arbitrary point of the domain. Then, the nodal values of the velocity corrections u' and v' are obtained by solving the discretized forms of the following equations

$$u' = \frac{\partial \phi}{\partial x}; \quad v' = \frac{\partial \phi}{\partial r} \tag{7}$$

3. Results and discussion

A parametric study is carried out on the effects of axial heat conduction on forced convection heat transfer in flows through circular microchannels. Three microchannel lengths L are considered, namely $25D_i, 50D_i$ and $100D_i$, where D_i is the internal diameter of the microchannel wall, together with three values of the outer diameter D_o, namely $2D_i, 3D_i$ and $5D_i$, corresponding to wall thicknesses w equal to $0.5D_i, D_i$ and $2D_i$, respectively. The working fluid is assumed to have constant thermophysical properties in the temperature range considered and a Prandtl number $Pr = 5$. Three values of the Reynolds number $Re = \rho_f u_{in} D_i/\mu_f$, where u_{in} is the uniform inlet velocity, are considered, namely, 50, 100 and 200, together with two values of the ratio of the solid wall to fluid thermal conductivities, corresponding to $k_s/k_f = 25$ and 250. These two values have been chosen because they are representative of a condition where, if the fluid is water, the microchannel wall is made of stainless steel ($k_s/k_f = 25$) or of silicon ($k_s/k_f = 250$).

The external microchannel wall is heated with an axially constant heat flow rate per unit length q'_o which, to allow comparisons among different test cases, is assumed to be the same for all the geometries. This implies that the actual uniform heat flux $q''_o = q'_o/(\pi D_o)$ applied on the external surface depends on the outer diameter of the microchannel. To show the effects of possible heat losses through both end sections of the microchannel, convective boundary conditions are applied on these surfaces and equivalent convective heat transfer coefficients h_a are assumed such that the values of the end section Nusselt number are $Nu_e = h_a D_i/k_f = 0$ (adiabatic wall), 1 and 10. The end heat losses at the upstream and downstream end sections are assumed to take place towards environments whose temperatures t_a are equal to the inlet and outlet mean bulk temperatures of the fluid, respectively, as it would happen if there were entrance and exit manifolds. Accordingly, the temperatures $t_a = t_{b,in} = t_{in}$ and $t_a = t_{b,out}$ are assumed at the upstream and downstream sides, where t_{in} is the uniform inlet temperature of the fluid and $t_{b,out}$ is the mean bulk temperature at the outlet of the microchannel. Since, because of end heat losses, $t_{b,out}$ cannot be estimated "a priori", the solution must be obtained by an iterative procedure where, at each step, an updated value of $t_{b,out}$ is assumed until convergence is reached. A sketch of the computational domain, showing the imposed thermal boundary conditions, is reported in Fig. 1.

As stated above, two different domains are considered in the solution for velocity and thermal fields. The one-dimensional axisymmetric domain where the parabolized Navier–Stokes equations are integrated is discretized using 80 linear elements, with sizes gradually increasing with increasing distance from the walls, while the two-dimensional axisymmetric domains where the energy equation is integrated are discretized using non-uniform grids of 4-node bilinear elements with 60 subdivisions (30 of which in the fluid) in the radial direction and between 150 (for $L = 25D_i$) and 384 (for $L = 100D_i$) subdivisions in the axial direction, with a total number of nodes ranging from 9211 to 23485. Preliminary tests have shown that these meshes are fine enough to yield grid independent results.

The computed results used in the present analysis include axial distributions of the dimensionless bulk temperature T_b, of the inner wall dimensionless temperature T_i, where the dimensionless temperature is defined as $T = \pi k_f (t - t_{in})/q'_o$, and of the local Nusselt number

$$Nu = \frac{h_i D_i}{k_f} = \frac{q''_i D_i}{(t_i - t_b)k_f} \tag{8}$$

where h_i and q''_i are the local convective heat transfer coefficient and heat flux at the inner surface of the microchannel and t_i and t_b are

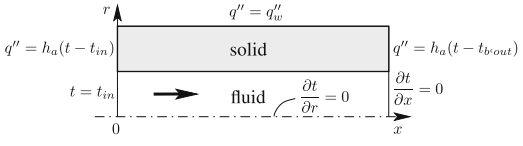

Fig. 1. Computational domain (not to scale) and thermal boundary conditions.

the corresponding wall and bulk temperatures. The length averaged Nusselt number

$$\overline{Nu} = \frac{1}{L}\int_0^L Nu\, dx \tag{9}$$

is also computed.

The important components of the procedure illustrated above have already been extensively validated in the past. In particular, the finite element code employed for the solution of the parabolized Navier–Stokes equations has been thoroughly tested and validated through comparisons of calculated results with available literature data (Nonino et al., 1988, 2006). Instead, the code used for the solution of the energy equation in two- and three-dimensional domains is part of a procedure, described by Nonino and Comini (1997), which also solves the elliptic form of the Navier–Stokes equations and whose validity has been proved by Nonino and Croce (1997). Finally, the complete procedure described in this paper has been validated by comparing, for selected microchannels, the calculated temperature distributions with those obtained by solving, on the same grid, the full set of Navier–Stokes and energy equations in their elliptic form by means of a reliable and thoroughly tested finite element code (Nonino and Comini, 1997; Nonino and Croce, 1997). As an example, comparisons of the axial distributions of the dimensionless wall and bulk temperatures and of the local Nusselt numbers obtained with the hybrid and with the fully elliptic procedures are shown in Fig. 2 for the case $Re = 200, L/D_i = 25, D_o/D_i = 3, k_s/k_f = 25$ and $Nu_e = 0$. It must be noticed that this probably represents one of the most critical test cases, among those considered here, since the hydrodynamic entrance region extends for a significant part of the microchannel due to the combination of a high Reynolds number and a short duct length. The agreement of the results yielded by the two procedures is excellent and, actually, the two curves for T_b are indistinguishable in Fig. 2. The same type of agreement has been found in all the other tests not reported here for the sake of brevity.

A total of 162 computer simulations have been carried out to allow for all possible combinations of the values of the above parameters. Moreover, additional simulations concerning the corresponding test cases with zero wall thickness ($w/D_i = 0$, i.e., $D_o/D_i = 1$) have also been carried out for comparison purposes, since this case corresponds to the classical H thermal boundary condition (Shah and London, 1978). To keep the size of the paper within reasonable limit, the effects of axial heat conduction on local values of relevant parameters (Nu, T_i and T_b) are shown here only with reference to some of the tests, while all the results are used to illustrate its effects on global parameters such as $\overline{Nu}$.

3.1. Influence of the wall thermal conductivity

It is well known (Maranzana et al., 2004; Hetsroni et al., 2005; Li et al., 2007) that the effects of axial heat conduction are more relevant in case of short ducts, thick walls and low Reynolds numbers. Therefore the influence of the wall thermal conductivity is shown here with reference to the case $L/D_i = 25, D_o/D_i = 5$, $Re = 50$ and $Nu_e = 0$. In Fig. 3, axial distributions of the local Nusselt number are reported for $k_s/k_f = 25$ and 250, together with that pertaining to the microchannel with $D_o/D_i = 1$, shown as a reference. The dimensionless axial coordinate is defined as $X^* = x/(D_i Pe)$ (Shah and London, 1978). A logarithmic scale is used for X^* in Fig. 3a to show the influence of the wall thermal conductivity in the part of the microchannel near the inlet, while a linear scale is used in Fig. 3b to better illustrate its influence in the last part. It is apparent that axial wall heat conduction has the generalized effect of reduc-

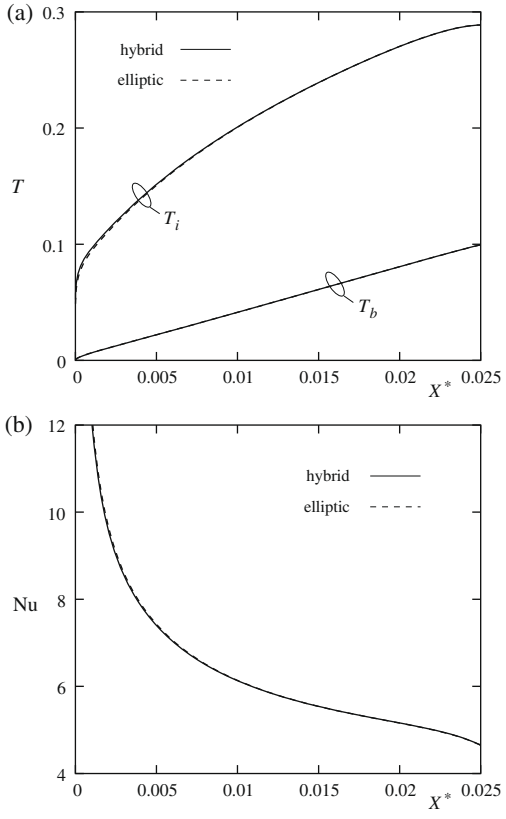

Fig. 2. Comparisons of results yielded by the hybrid and the fully elliptic procedures for $Re = 200, L/D_i = 25, D_o/D_i = 3, k_s/k_f = 25$ and $Nu_e = 0$: (a) axial distributions of the dimensionless wall temperature T_i and bulk temperature T_b; (b) axial distributions of the local Nusselt number Nu.

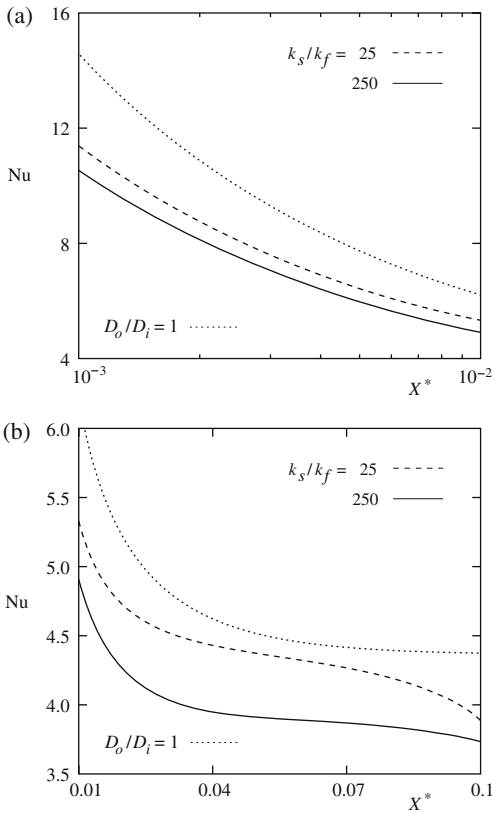

Fig. 3. Local Nusselt number axial distributions for $L/D_i = 25, D_o/D_i = 5, Re = 50, Nu_e = 0$ and the considered values of k_s/k_f: (a) $10^{-3} \leqslant X^* \leqslant 10^{-2}$ (logarithmic scale) and (b) $10^{-2} \leqslant X^* \leqslant 10^{-1}$ (linear scale).

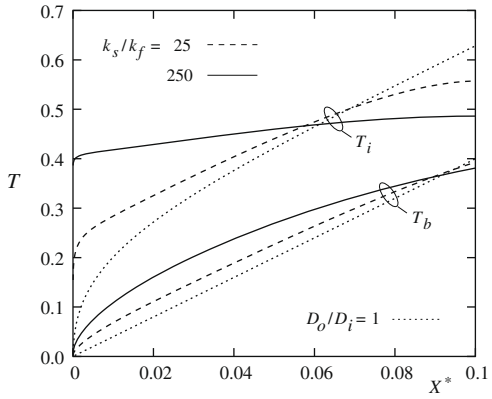

Fig. 4. Axial distributions of the dimensionless wall temperature T_i and bulk temperature T_b for $L/D_i = 25, D_o/D_i = 5, Re = 50, Nu_e = 0$ and the considered values of k_s/k_f.

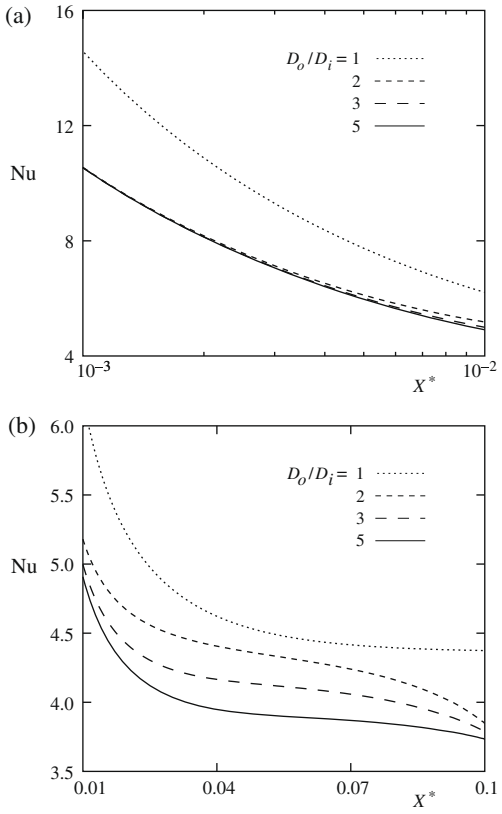

Fig. 5. Local Nusselt number axial distributions for $L/D_i = 25, Re = 50, k_s/k_f = 250, Nu_e = 0$ and the considered values of D_o/D_i: (a) $10^{-3} \leqslant X^* \leqslant 10^{-2}$ (logarithmic scale) and (b) $10^{-2} \leqslant X^* \leqslant 10^{-1}$ (linear scale).

ing the local Nusselt number with respect to the reference value corresponding to $D_o/D_i = 1$ and that larger reductions are found for larger values of k_s/k_f. Moreover, the decrease of the Nusselt number is more significant near the entrance and exit of the microchannel than in the intermediate part. Similar plots, not reported here, concerning smaller values of D_o/D_i show a similar behaviour. However, while the corresponding values of Nu for small X^* are nearly the same as those shown in Fig. 3a, the values of Nu for larger X^* are not as small as the ones reported in Fig. 3b. The axial distributions of the dimensionless wall and bulk temperatures corresponding to the cases illustrated in Fig. 3 are reported in Fig. 4. The influence of the wall thermal conductivity is evident. In particular, an increase of the ratio k_s/k_f leads to a more uniform streamwise temperature distribution at the fluid–solid interface, which, for very high values of k_s/k_f, would approach that corresponding to the classical T boundary condition (Shah and London, 1978).

3.2. Influence of the wall thickness

The influence of the wall thickness can also be illustrated with reference to the case $L/D_i = 25, Re = 50$ and $Nu_e = 0$. The axial distribution of the local Nusselt number is reported in Fig. 5 for $k_s/k_f = 250$ and different values of D_o/D_i. Again, a logarithmic scale for X^* is used in Fig. 5a to show the influence of the wall thickness in the part of the microchannel near the entrance, while a linear scale is used in Fig. 5b to better illustrate its influence in the last part. A comparison of Figs. 3b and 5b shows that an increase of the wall thermal conductivity has an effect on the axial distribution of the local Nusselt number which, along the most part of the microchannel, is similar to that of an increase of the wall thickness. In fact, lower values of Nu are found for increasing values of both wall thermal conductivity and wall thickness. However, in Fig. 5a it is apparent that for small values of X^*, with a given wall thermal conductivity, the values of the local Nusselt number are nearly independent of the wall thickness (as long as this does not tend to zero), while according to Fig. 3a, with a given wall thickness, the dependence of Nu on wall thermal conductivity remains significant even very near the microchannel inlet. Results of other test cases (not reported here), carried out using other values of the ratio k_s/k_f, show qualitatively similar behaviours.

3.3. Entrance effects

The combination of channel entrance and axial heat conduction effects is best illustrated with reference to the test cases with $L/D_i = 100$, $Nu_e = 0$, $k_s/k_f = 250$ and different values of D_o/D_i and Re. With reference to these combinations of parameters, axial distributions of the local Nusselt number are reported in Fig. 6a for $Re = 50$, i.e., $Pe = 250$, and Fig. 6b for $Re = 200$, i.e., $Pe = 1000$. Fig. 6a demonstrates that, contrary to the common experience, when the entrance length is rather small compared to the total length of the microchannel (low Reynolds and Péclet numbers) and axial heat conduction is significant, the local Nusselt number does not monotonically decrease from inlet to outlet, but presents a local minimum in the first part of the microchannel. On the other hand, such minima also appear in some of the local Nusselt number axial distributions obtained numerically by Lelea (2007) and experimentally by Lelea et al. (2004). On the contrary, with higher values of the Reynolds and Péclet numbers, that is, with larger entrance lengths, more usual trends of monotonically decreasing local Nusselt numbers in the axial direction are found, as shown in Fig. 6b. Intermediate behaviours are found for $L/D_i = 50$ or $Re = 100$ (plots not reported here). If k_s/k_f is equal to 25, instead, no minima in local Nusselt number axial distributions are found for any of the Reynolds numbers or of the ratios D_o/D_i considered.

3.4. Effects of end losses

The effects on the local Nusselt number of heat losses at microchannel ends, combined with those of the axial heat conduction in the microchannel walls, are rather complex. Some examples are shown in Fig. 7, where axial distributions of the local Nusselt number are reported for the cases with $L/D_i = 25, D_o/D_i = 2, Re = 50$ and the values of k_s/k_f and of the end section Nusselt number considered, and in Fig. 8, where similar plots are reported, but with reference to $D_o/D_i = 5$. As can be seen in Figs. 7a and 8a, with $k_s/k_f = 25$ the main effect of the end heat losses is represented

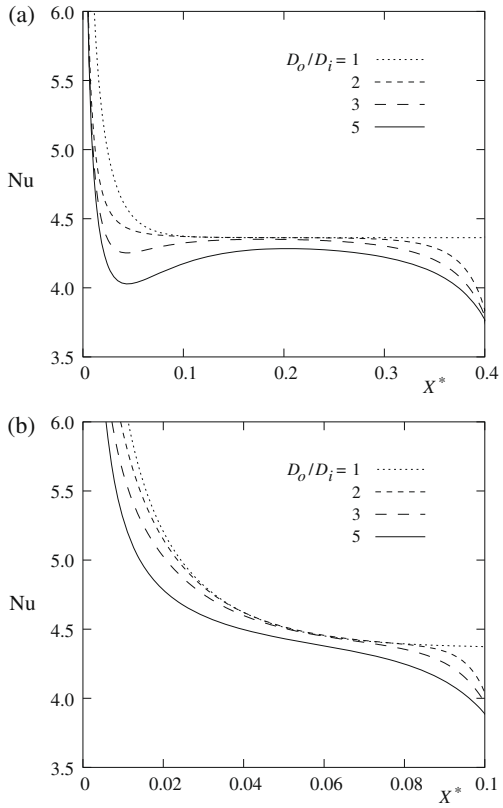

Fig. 6. Local Nusselt number axial distributions for $L/D_i = 100, k_s/k_f = 250, Nu_e = 0$ and the considered values of D_o/D_i: (a) $Re = 50$ and (b) $Re = 200$.

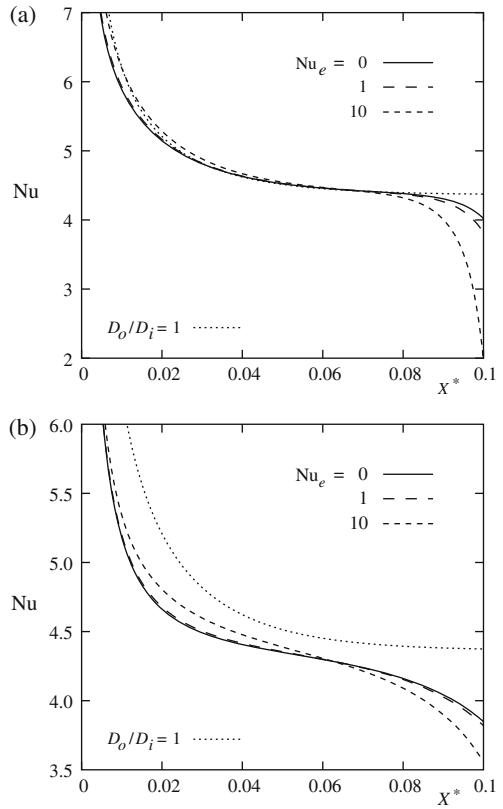

Fig. 7. Local Nusselt number axial distributions for $L/D_i = 25, D_o/D_i = 2, Re = 50$ and the considered values of Nu_e: (a) $k_s/k_f = 25$ and (b) $k_s/k_f = 250$.

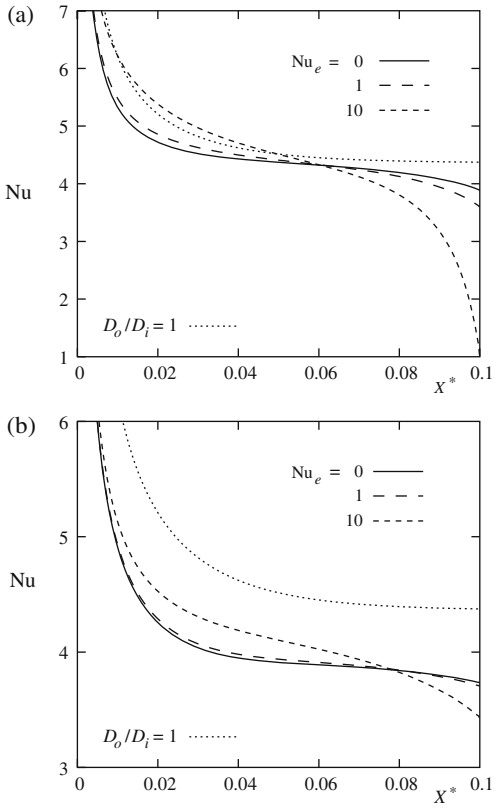

Fig. 8. Local Nusselt number axial distributions for $L/D_i = 25, D_o/D_i = 5, Re = 50$ and the considered values of Nu_e: (a) $k_s/k_f = 25$ and (b) $k_s/k_f = 250$.

by an increase of the local Nusselt number with respect to the case with adiabatic ends ($Nu_e = 0$) in the first part of the microchannel and in a reduction near the microchannel exit. A similar effect, but not as evident, can also be observed in Figs. 7b and 8b for $k_s/k_f = 250$. To allow a better interpretation of the results shown in Figs. 7 and 8, the values (in percentage) of the ratio q_e/q_o of the total microchannel end heat losses q_e over the total heat flow rates at the external microchannel surfaces $q_o = q'_o L$ are reported in Table 1 for the test cases with $Nu_e > 0$. Finally, to give more insight into the complex heat transfer effects related to the heat losses through the end sections of microchannel walls, the axial distributions of the dimensionless wall and bulk temperatures corresponding to the cases illustrated in Figs. 7 and 8 are reported in Figs. 9 and 10.

3.5. Characterization of axial heat conduction effects

The so-called axial conduction number M, defined as the ratio of the nominal axial heat transfer rate by conduction in the wall $q_{cond//}$ to the heat transfer rate by convection in the fluid q_{conv},

Table 1
Microchannel end heat losses for the test cases with $Nu_e > 0$ referred to in Figs. 7 and 8.

D_o/D_i	k_s/k_f	Nu_e	q_e/q_o (%)
2	25	1	1.0
2	25	10	6.6
2	250	1	1.2
2	250	10	10.1
5	25	1	9.1
5	25	10	34.2
5	250	1	10.9
5	250	10	51.2

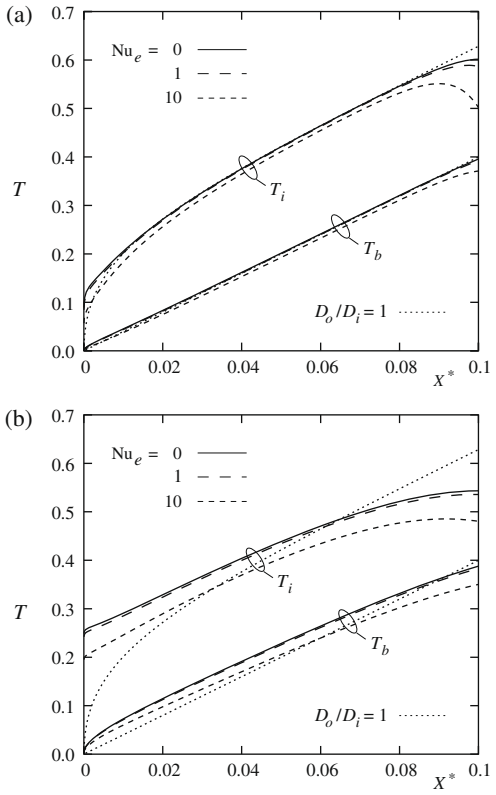

Fig. 9. Axial distributions of the dimensionless wall and bulk temperatures for $L/D_i = 25, D_o/D_i = 2, Re = 50$ and the considered values of Nu_e: (a) $k_s/k_f = 25$ and (b) $k_s/k_f = 250$.

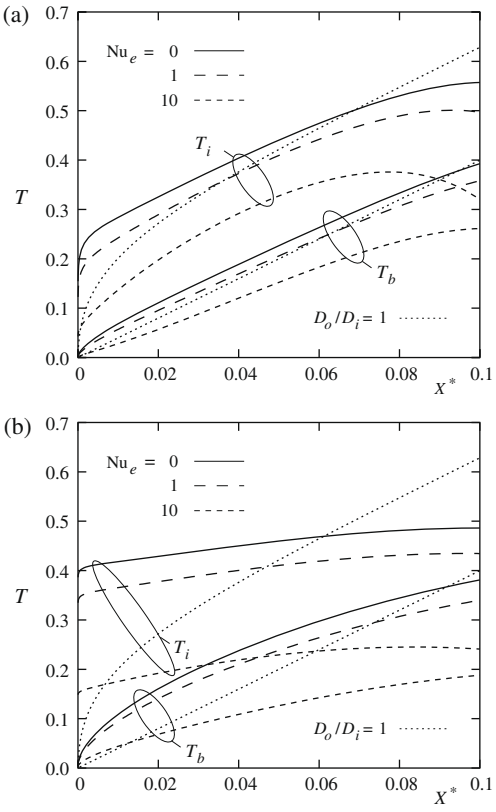

Fig. 10. Axial distributions of the dimensionless wall and bulk temperatures for $L/D_i = 25, D_o/D_i = 5, Re = 50$ and the considered values of Nu_e: (a) $k_s/k_f = 25$ and (b) $k_s/k_f = 250$.

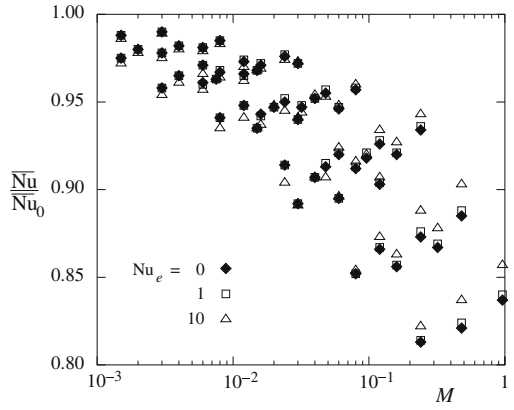

Fig. 11. Ratio of the length averaged Nusselt numbers $\overline{Nu}$ over the corresponding values $\overline{Nu}_0$, pertaining to microchannels with wall thickness equal to zero, as a function of the axial conduction parameter M.

$$M = \frac{q_{cond//}}{q_{conv}} = \left(\frac{k_s}{k_f}\right)\left(\frac{D_o^2 - D_i^2}{D_i L}\right)\frac{1}{Re\ Pr} \tag{10}$$

is often used to express the relative importance of the axial heat conduction in the tube wall with respect to the convective heat transfer in the fluid (Maranzana et al., 2004; Hetsroni et al., 2005; Celata et al., 2006; Morini, 2005; Gamrat et al., 2005; Li et al., 2007). With the values of the parameters adopted in this study, M varies in the range from 0.00075 to 0.96, thus including the critical lower limits of about 0.01 or 0.02, commonly accepted for axial heat conduction to be significant (Hetsroni et al., 2005; Celata et al., 2006; Morini, 2005).

Fig. 11 shows a plot of the values of the ratio of the length averaged Nusselt numbers $\overline{Nu}$, pertaining to all the test cases considered, and $\overline{Nu}_0$, pertaining to the corresponding microchannels with wall thickness equal to zero ($D_o/D_i = 1$), as a function of the axial conduction parameter M. Different symbols are used to identify the results pertaining to different end section Nusselt numbers at the microchannel end sections. It clearly appears that, as already observed, the general effect of the axial heat conduction is a reduction of the average Nusselt number with respect to that corresponding to the classical H boundary condition (Shah and London, 1978) and that this reduction is smaller when there are heat losses at the microchannel ends ($Nu_e > 0$). It is also evident that, in general, the larger the value of M is, the larger the axial heat conduction effects are. However, it must also be noticed that the points in Fig. 11 tend to form a cloud rather than a curve and that the reduction of $\overline{Nu}$ with respect to $\overline{Nu}_0$ can be larger than 5% even for values of M lower than the limits indicated in the literature for axial heat conduction to be significant, i.e., 0.01 according to Hetsroni et al. (2005) and Celata et al. (2006) or 0.02 according to Morini (2005). All this confirms that, as already observed by Li et al. (2007), "M is not the only criterion for judging whether the axial heat conduction can be neglected".

4. Conclusions

The effects of axial heat conduction in the solid walls of microchannels of circular cross-sections have been analyzed with reference to the simultaneously developing flow of a constant property fluid in microchannels of different length, wall thickness and wall material, heated with a uniform heat flux at the outer surface, for different values of the Reynolds number. A hybrid finite element procedure, which implies the step-by-step solution of the parabolized momentum equations in the fluid domain, followed by the solution of the energy equation in the entire domain, correspond-

ing to both the solid and the fluid parts, has been used for the numerical simulations.

The influences of wall thermal conductivity, wall thickness, entrance effects and heat losses through the end sections of microchannel walls have been investigated and the reliability of a commonly used criterion, based on the so-called axial conduction number, for judging whether the axial heat conduction can be neglected has been discussed.

Acknowledgement

This work was funded by MIUR (PRIN/COFIN 2005 and 2007 projects).

References

Al-Bakhit, H., Fakheri, A., 2005. A hybrid approach for full numerical simulation of heat exchangers. In: Proceedings of the 2005 ASME Heat Transfer Summer Conference.

Al-Bakhit, H., Fakheri, A., 2006. Numerical simulation of heat transfer in simultaneously developing flows in parallel rectangular ducts. Appl. Therm. Eng. 26, 596–603.

Celata, G.P., Cumo, M., Marconi, V., McPhail, S.J., Zummo, G., 2006. Microtube liquid single-phase heat transfer in laminar flow. Int. J. Heat Mass Trans. 49, 3538–3546.

Fakheri, A., Al-Bakhit, H., 2005. Entrance and wall conduction effects in parallel flow exchangers. In: Proceedings of the 5th International Conference on Enhanced, Compact and Ultra-Compact Heat Exchangers: Science, Engineering and Technology.

Gamrat, G., Favre-Marinet, M., Asendrych, D., 2005. Conduction and entrance effects on laminar liquid flow and heat transfer in rectangular microchannels. Int. J. Heat Mass Trans. 48, 2943–2954.

Gresho, P.M., 1990. On the theory of semi-implicit projection methods for viscous incompressible flow and its implementation via a finite element method that also introduces a nearly consistent mass matrix. Part I: theory. Int. J. Numer. Meth. Fluid 11, 587–620.

Herwig, H., Hausner, O., 2003. Critical view on new results in micro-fluid mechanics: an example. Int. J. Heat Mass Trans. 46, 935–937.

Hetsroni, G., Mosyak, A., Pogrebnyak, E., Yarin, L.P., 2005. Heat transfer in microchannels: comparison of experiments with theory and numerical results. Int. J. Heat Mass Trans. 48, 5580–5601.

Hirsh, C., 1988. Numerical computation of internal and external flows, vol. 1. Wiley, New York.

Lelea, D., Nishio, S., Takano, K., 2004. The experimental research on microtube heat transfer and fluid flow of distilled water. Int. J. Heat Mass Trans. 47, 2817–2830.

Lelea, D., 2007. The conjugate heat transfer of the partially heated microchannel. Heat Mass Trans. 44, 33–41.

Li, Z., He, Y.-L., Tang, G.-H., Tao, W.-Q., 2007. Experimental and numerical studies of liquid flow and heat transfer in microtubes. Int. J. Heat Mass Trans. 50, 3447–3460.

Liu, Z.-G., Liang, S.-Q., Takei, M., 2007. Experimental study on forced convective heat transfer characteristics in quartz microtube. Int. J. Therm. Sci. 46, 139–148.

Maranzana, G., Perry, I., Maillet, D., 2004. Mini- and micro-channels: influence of axial conduction in the walls. Int. J. Heat Mass Trans. 47, 3993–4004.

Mori, S., Sakakibara, M., Tanimoto, A., 1974. Steady heat transfer to laminar flow to a circular tube with conduction in the tube wall. Heat Trans.– Jpn. Res. 3, 37–46.

Morini, G.L., 2005. Viscous dissipation as scaling effect for liquid flows in microchannels. In: Proceedings of the 3rd International Conference on Microchannels and Minichannels.

Nonino, C., Del Giudice, S., Comini, G., 1988. Laminar forced convection in three-dimensional duct flows. Numer. Heat Trans. 13, 451–466.

Nonino, C., Comini, G., 1997. An equal-order velocity-pressure algorithm for incompressible thermal flows. Part 1: formulation. Numer. Heat Trans. – Part B 32, 1–15.

Nonino, C., Croce, G., 1997. An equal-order velocity-pressure algorithm for incompressible thermal flows. Part 2: validation. Numer. Heat Trans. – Part B 32, 17–35.

Nonino, C., 2003. A simple pressure stabilization for a SIMPLE-like equal-order FEM algorithm. Numer. Heat Trans. Part B 44, 61–81.

Nonino, C., Del Giudice, S., Savino, S., 2006. Temperature dependent viscosity effects on laminar forced convection in the entrance region of straight ducts. Int. J. Heat Mass Trans. 49, 4469–4481.

Patankar, S.K., 1980. Numerical Heat Transfer and Fluid Flow. Hemisphere, Washington DC.

Ryu, J.H., Choi, D.H., Kim, S.J., 2002. Numerical optimization of the thermal performance of a microchannel heat sink. Int. J. Heat Mass Trans. 45, 2823–2827.

Shah, R.K., London, A.L., 1978. Laminar Flow Forced Convection in Ducts. Academic Press, New York.

Tiselj, I., Hetsroni, G., Mavko, B., Mosyak, A., Pogrebnyak, E., Segal, Z., 2004. Effect of axial conduction on the heat transfer in micro-channels. Int. J. Heat Mass Trans. 47, 2551–2565.